This is a preprint, the final version is subject to change, of the American Mineralogist (MSA)
Cite as Authors (Year) Title. American Mineralogist, in press.
(DOI will not work until issue is live.) DOI: http://dx.doi.org/10.2138/am-2017-5719

American Mineralogist 5719 Revision 2

High-pressure high-temperature Raman spectroscopy of kerogen: relevance to subducted organic carbon

Laurel B. Childress[1,*] and Steven D. Jacobsen[1]
[1]*Northwestern University, Department of Earth and Planetary Sciences, Evanston IL, 60208 USA*

ABSTRACT

The amount of insoluble macromolecular organic matter in the Earth's crust, commonly referred to as kerogen, far exceeds the mass of living organic matter. The fraction of kerogen in sediments subducted into the mantle remains poorly constrained, and will vary depending on the physical-chemical properties of kerogen along different slab geotherms. We studied the pressure-temperature evolution of carbon vibrational frequencies in isolated kerogen, previously not subjected to metamorphism, using Raman spectroscopy in a sapphire optical cell up to 3.2 GPa and 450 °C, corresponding to colder subduction geotherms. For blue-green laser excitation, we find optical irradiance exceeding ~3 kW/cm^2 induces changes in spectral features of the primary graphitic (G-band) and two main disordered modes (D1 and D2) that might otherwise be mistaken for thermal maturation. Whereas previous in situ studies have investigated the changes in these molecular vibrations of kerogen at high temperature or high pressure, we collected Raman spectra of isolated kerogen at simultaneous high P-T conditions. Although instantaneous and irreversible changes in band ratios of isolated kerogen were observed above ~350 ˚C at room pressure, long-duration (2-8 hour) heating experiments at 450 ˚C and 2.7-3.0 GPa reveal no permanent change in band structure. The reduction in vibrational frequencies of the disordered carbon modes with temperature (dv/dT) at pressures >1 GPa is slightly less than found at room pressure, further indicating that pressure effectively increases the thermal stability of kerogen. Our results suggest that kerogen reaching depths of 60 km where the temperature is below ~450 °C may subduct into the mantle, providing a potential source for the organic-rich component of carbon recently detected in certain upper mantle diamonds.

Email: lbchildr@u.northwestern.edu

INTRODUCTION

The transport, burial, and transformation of organic carbon along active margins is an important but still poorly constrained component of the global biogeochemical carbon cycle. Along active continental-oceanic tectonic boundaries associated with small mountainous rivers, such as Cascadia, Alaska, Taiwan, and South America, exported kerogen (fossil carbon) often dominates riverine sediments, and can constitute as much, and potentially more than 75% of the total particulate organic load (Leithold et al. 2006; Drenzek et al. 2009; Blair et al. 2010; Hilton et al. 2010). High sediment transport rates, coupled with close proximity to sediment sources, promotes the efficient burial and preservation of organic carbon in the marine environment. Kerogen forms by diagenetic to metasomatic processes imposed on organic matter, resulting in a highly recalcitrant and structurally complex compound capable of persisting in the sedimentary record on geologic time scales and likely exceeding the mass of carbon in living organic matter by four orders of magnitude (Durand 1980). Understanding the high-pressure, high-temperature properties of kerogen will lead to a better understanding of the behavior of kerogen during subduction.

Raman spectroscopy has been widely used to characterize carbonaceous material (CM) in Earth and planetary materials for some time. Detection of biosignatures in CM is a primary focus in the study of early life on Earth (Pasteris and Wopenka 2002; Schopf et al. 2002; Schopf and Kudryavtsev 2005; Kremer et al. 2012) with potential application to Mars (e.g. Ellery et al. 2004; Dunn et al. 2007; Dartnell et al. 2012; Steele et al. 2012), where the ExoMars rover, expected to launch in 2018, will deploy a Raman spectrometer to analyze potential organic compounds using a 532 nm continuous excitation wavelength (Courrèges-Lacoste et al. 2007; Rull et al. 2013; Hutchinson et al. 2014). Characterization of CM by Raman spectroscopy has also been used to

infer the thermal history of meteorites (Quirico et al. 2003; Hochleitner et al. 2004; Bonal et al. 2006; Busemann et al. 2007; Matsuda et al. 2010) and interplanetary dust particles (Wopenka 1988; Sandford et al. 2006), as well as to characterize riverine particulate organic carbon (Galy et al. 2007, 2008; Bouchez et al. 2010). Interpretation of CM Raman spectra in Earth and planetary materials requires caution because of its sensitivity to the laser (Kagi et al. 1994; Morishita et al. 2011), ionizing radiation (Dartnell et al. 2012) and polishing in sample preparation (Ammar et al. 2011).

In terrestrial meta-sedimentary rocks, the evolution of CM crystallinity measured by Raman spectroscopy has been used to develop a geothermometer of peak metamorphic temperature in the 300-700 °C range (Wopenka and Pasteris 1993; Beyssac et al. 2002a, 2002b; Rahl et al. 2005). Application to lower grade metamorphism or metasomatism at 25-300 °C is not as well developed, although there has been recent progress (Lahfid et al. 2010). In general, thermometry studies rely on the influence of temperature on Raman spectra of the ordered G (graphite) band at ~1580 cm^{-1} and disordered or defect bands, D1 (1350 cm^{-1}) and D2 (1620 cm^{-1}). Because the two primary defects bands are absent in well-crystallized graphite, the evolution of ratios R1 = $[D1/G]_{intensity}$ and R2 = $[D1/(G+D1+D2)_{area}]$ estimate the degree to which graphitic ordering has occurred. In metamorphic belts, there is a strong correlation between the R2 ratio and peak metamorphic temperature based on mineral assemblages (e.g. Beyssac et al. 2002b).

Whereas geothermometry of CM in metasediments examines CM that has been subjected to simultaneous pressures and temperatures on geologic timescales, experiments can only examine essentially instantaneous effects. The graphitization of CM has been studied in heating experiments (e.g. Beny-Bassez and Rouzaud 1985; Rouzaud and Oberlin 1989). Because the effect of pressure promotes the graphitization process, metamorphic samples display

graphitization features at significantly lower temperatures than can be reproduced in the laboratory (Huang et al. 2010). Furthermore, laboratory heating experiments up to 600 °C on kerogen not previously subjected to regional metamorphism showed complete reversibility in the temperature dependence of the Raman shift of G, D1, and D2 bands to lower wavenumbers (Huang et al. 2010), despite evidence for bond-breaking changes associated with changes in the intensity ratio of D2/G bands above ~350 °C (Huang et al. 2010). Pressure shifts the first-order bands of kerogen in the opposite sense, to higher wavenumbers, so it might be expected that simultaneous pressure and temperature will influence the temperature effect differently than at room pressure. Although some experiments have examined the effect of pressure and temperature on kerogen Raman spectra post-heating ex situ (e.g. Beyssac et al. 2003a), the evolution of kerogen Raman has not yet been explored at simultaneous high pressures and high temperatures.

Characterizing the evolution of CM in mixtures of marine and terrestrial sediments in near-shore sediments at subduction zones has the potential to constrain fluxes of organic carbon removal from the biosphere (e.g. Mackenzie et al. 2004; Hayes and Waldbauer 2006). However, primarily because CM is dark brown to black and highly absorbing of typical Raman-laser excitation wavelengths, it is imperative to characterize the influence of laser-induced heating on interpretation of the character of CM Raman spectra (Everall et al. 1991; Kagi et al. 1994; Morishita et al. 2011).

In this study, we first examined the effect of laser-induced heating by the Raman excitation source in the blue-green region (458 nm) on the evolution of Raman D and G bands of kerogen. We examine isolated kerogen extracted from rocks of an accreted shale-rich mélange at laser powers ranging from 0.05 to 6 mW, and compare the laser-heating effects to controlled

heating over the temperature range of 25-500 °C using a laser power below the damage threshold, determined in the first part of the study. To study the effect of pressure on the high-temperature stability and vibrational properties of kerogen, we measured first-order Raman spectra at simultaneous *P-T* conditions up to 3.2 GPa and ~400 °C, within the range of colder subduction geotherms where kerogen is most likely to persist to deeper depths. The spectra were analyzed for the P-T evolution of primary vibrational band widths, intensities, and ratios in order to shed light on the molecular evolution of carbon along *P-T* paths typical of subduction environments.

METHODS

Kerogen was extracted by HF methods (Durand and Nicaise 1980) from fine-grained, shale-rich mélange (Franciscan Complex) of the Eel River watershed in northern California (Blair et al. 2003). Although this extraction can potentially alter or dissolve some organic compounds (Durand and Nicaise 1980), these effects were minimized by the maturity of sample and room-temperature digestion in an inert atmosphere. Although part of the uplifted accretionary wedge material associated with the coastal mountain region, the kerogen examined in this study has experienced little if any metamorphic-grade alteration (Blair et al. 2004; Leithold et al. 2006). The mature, isolated kerogen used in this study exhibits first-order D and G-bands very similar to petrogenic carbon from riverine sediment loads (Galy et al. 2008; Bouchez et al. 2010).

Raman spectra were obtained using 458 nm solid-state diode laser (Melles Griot BLS 85-601) with ~250 mW output power at the source. A custom-built optical system was constructed around an Olympus BX microscope with confocal apertures before and after the sample. Spectra

126 were obtained using a 0.3 m Andor Shamrock spectrograph with a 60 μm entrance slit and 1200
127 lines per mm diffraction grating. The Andor Newton DU970-CCD camera was
128 thermoelectrically cooled to -90 °C. Spectra were collected using either a 100x Mitutoyo M Plan
129 Apo objective with 6 mm working distance and 0.7 numerical aperture (Figure 1 and laser
130 heating experiments) or an extra-long working distance 20x Mitutoyo M Plan Apo objective with
131 20.2 mm working distance and 0.42 numerical aperture (all other measurements). The laser
132 power at the sample was always measured using a hand-held power meter with ±0.01 mW
133 precision near the ~2 μm diameter focal spot of the objective. For the spectra collected to study
134 the effects of laser heating, laser powers ranged from 0.05 to 20 mW, as measured at the sample
135 position. In the laser heating experiments, the focused laser was held steady on the sample for 5
136 minutes prior to data collections of 120 seconds, averaged over three accumulations.
137 High-temperature experiments at room pressure were performed using a resistive heater,
138 where the sample was placed on the flat culet of a diamond anvil mounted in a tungsten carbide
139 seat wound with a Mo-wire resistive heater. The sample was placed directly on the culet of the
140 diamond anvil with Ar gas flowing over the sample. A K-type thermocouple attached to the
141 diamond was used to monitor the temperature, which was increased at 25 °C intervals and held
142 for 10 minutes at each temperature prior to data collection for three accumulations of 60 seconds.
143 Simultaneous high-pressure, high-temperature experiments were performed using a
144 resistively-heated sapphire-anvil cell. Due to overlap of the first-order longitudinal phonon of
145 diamond at 1332 cm^{-1}, sapphire anvils were required to obtain kerogen Raman spectra at high
146 pressures. We used sapphire anvils of 3.1 mm diameter and 1.7 mm height with 300 or 400 μm
147 culet sizes. The 400-μm culet anvils routinely cracked at high temperature above about 2 GPa, so

we used 300-μm culets to reach 3.2 GPa maximum pressure at high temperature without breakage. The isolated kerogen samples were loaded with a KBr pressure medium into 0.20 mm thick Inconel gaskets, pre-indented to 0.15 mm thickness with sample chambers drilled at about half the diameter of the culet. Pressures were determined using the Sm:YAG scale (Trots et al. 2013). The nominal precision in all pressure measurements is ±0.1 GPa. K-type thermocouples attached to both upper and lower sapphire anvils were used to monitor the temperature, which was increased at 25-50 °C intervals and held at each temperature for 15 minutes prior to data collection lasting 60 seconds accumulated three times. For long-duration heating experiments, we increased the pressure to ~3 GPa and heated the same sample to 450 ˚C for periods lasting 2-8 hours, returning to room temperature in between each heating cycle. Laser power measured at the objective using a hand held power meter was 0.09 mW. Attenuation through the sapphire anvil resulted in a laser power of 0.05 mW at the sample, as measured using an open cell.

Deconvolution of the spectra was performed using PeakFit (Systat Software Inc.). Raman bands of kerogen are typically a combination of a Gaussian and Lorentzian fit, therefore a Voigt Amplitude function is often used (Beyssac et al. 2002b, 2003b; Rahl et al. 2005). Sadezky et al. (2005) demonstrate that first-order bands, with the exception of D3, are Lorentzian. We fitted spectra using both Voigt and Lorentzian fits, finding no significant difference in the results. All first order-bands in this study are reported using Lorentzian Amplitude and Area-based fits with standard errors reported from PeakFit.

RESULTS

Effect of laser heating on kerogen Raman spectra

Raman spectra of the kerogen in this study are characterized by first-order (1100 – 1800 cm^{-1}; Figure 1a) and second-order (2200 – 3500 cm^{-1}; Figure 1b) vibrational bands typical of mature kerogen (e.g. Wopenka and Pasteris 1993). Within the first-order region, the G band (1580 cm^{-1}) associated with C–C in-plane stretching of aromatic layers (e.g. Ferrari and Robertson 2000) overlaps with the D2 (1620 cm^{-1}) disordered carbon band. Also present in the first order region are the D1 (1350 cm^{-1}) and D3 (1500 cm^{-1}) bands (Beyssac et al. 2002b). The D bands, shown in Figure 1a, are attributed to a variety of graphitization disorder effects, including reduced graphite lattice symmetry near edges, edge vibrations, heteroatoms, and defects in or between the aromatic plane (Beny-Bassez and Rouzaud 1985; Wang et al. 1990; Beyssac et al. 2002a).

The second order region shows bands at approximately 2700, 2900, and 3250 cm^{-1} labeled S1, S2, and S3 in Figure 1b. These bands are attributed to overtones and combination of the first-order region (Kelemen and Fang 2001). The S1 band is possibly an overtone of the D1 band (2 x 1350 cm^{-1}), S2 a result of combination scattering from the D1 and G bands (1350 + 1580 cm^{-1}), and S3 an overtone of D2 (2 x 1620 cm^{-1}) (Marshall et al. 2009). Another explanation for the second order region is the presence of aliphatic or aromatic C–H stretching associated with the S2 band, which has been observed in shale samples (Tsu et al. 1978; Czaja et al. 2009; Marshall et al. 2009). In this study, we focus on the first-order Raman bands of kerogen.

Band intensity or area ratios are commonly used parameters for the assessment of thermal maturity or metamorphic grade (e.g. Wopenka and Pasteris 1993; Beyssac et al. 2002b; Huang et al. 2010). R1 is calculated as $[(D1/G)_{intensity}]$ and R2 is calculated by $[D1/(G + D1 + D2)_{area}]$ (Beyssac et al. 2002b; Huang et al. 2010). Wopenka and Pasteris (1993) note that R1 and R2 are

193 less reliable for the interpretation of kerogen metamorphic grade than FWHM, due to the fact
194 that more mature kerogen will have much narrower first order peaks coupled with stronger
195 second order features. Decreases in R1 and R2 provide evidence for increased thermal maturity
196 and metamorphic grade (Beyssac et al. 2002b). Another less commonly used parameter, R3, is
197 calculated by $[S2/(S1 + S2)_{area}]$, however with generally weaker bands in the second order region
198 for kerogen this parameter may not be sensitive to small changes (Beyssac et al. 2002b).
199 Additional quantitative measurements to indicate increased thermal maturity/metamorphic grade
200 include a decrease in the intensity of the D1 band, decrease in the area of the D1 band, decrease
201 in the area of the D3 band, narrowing of the G band, decrease in the intensity of the D2 band,
202 decrease in the intensity of the S2 band, shift in the G band to a lower center position (Beyssac et
203 al. 2002a).
204 Increasing the excitation laser power results in an overall decrease of normalized
205 intensity (Figure 2a), but can also clearly influence band intensity ratios, as illustrated in Figure
206 2b. Therefore, it is imperative to quantify the damage threshold of excitation lasers in Raman
207 studies of kerogen (e.g. Morishita et al. 2011). In order to characterize the heating potential of
208 the 458 nm excitation laser used in this study, we collected spectra under otherwise identical
209 collection conditions at various laser powers ranging from 0.05 to ~6 mW, as measured by a
210 Melles-Griot hand-held laser meter near the focal point of the objective lens. Spectra in Figure 2a
211 and 2b are shown only to 6 mW maximum power because at higher powers (up to 20 mW) the
212 sample instantaneously degraded. Figure 3 illustrates the effect of temperature (direct heating
213 under a stream of Ar gas) on the first-order Raman spectra of kerogen, measured using a laser
214 power of 0.05 mW.
215

Effect of temperature on kerogen Raman spectra

In order to compare the decrease of band intensities on heating by the laser and by direct heating, Figure 4 illustrates the normalized intensities of G, D1, and D2 bands as a function of laser power (normalized to intensity at 0.05 mW) and temperature (normalized to 22 °C, laser power of 0.05 mW). With increased laser power (Figure 4a) and increased direct thermal heating (Figure 4b) normalized intensities decrease, reflecting alteration and eventual degradation above ~6 mW and 525°C. While greater initial intensities may be achieved by increased laser power, as shown in Figure 4a between the 0.05 and 0.76mW step, prolonged exposure to increased laser power will damage the sample.

Figure 5a illustrates the influence of laser power on R1 (intensity) and R2 (area) ratios. Taking 0.05 mW as the reference, the R1 = $(D1/G)_{intensity}$ ratio decreases from approximately 0.9 to 0.65 with an increase in laser power to ~1.5 mW, but does not decrease significantly further up to 6 mW, suggesting the most drastic changes occur in R1 below 2 mW power. The R2 area ratio is somewhat invariant up to 2 mW but decreases by almost 50% at 3-6 mW laser power (Figure 5a). For comparison to temperature, we plot in Figure 5b the R1 ratio as a function of temperature up to 500 °C, where the drastic drop in R1 from ~0.9 to ~0.6 is observed above approximately 300 °C, implying that 1-2 mW of laser power can cause an equivalent of 300 °C heating. The drastic decrease in R1 upon raising the laser power from 0.05 mW to greater than 1 mW (Fig 5a) suggests that a practical laser-damage threshold for 458 nm is significantly below 1mW.

Figure 6 illustrates the effect of laser power on D1, D2, and G-band widths, expressed as full-width at half maximum (FWHM, cm^{-1}). The G and D1 bands (Fig. 6a, b) both decrease in FWHM with increasing laser power, while the disordered carbon band D2 (Fig. 6c) increases. As

a function of temperature (Figure 6 d-f) all bands show an increase in FWHM with increasing temperature. The increase in FWHM is largest in the D2 band (Figure 6f), however the majority of band width increase does not occur until temperatures greater than 400˚C.

The most robust comparison of laser-heating to direct heating below the laser-damage threshold can be seen in G, D1, and D2 peak positions. Figure 7a overlays the shift in band positions with both laser power and temperature. Whereas the D1 peak position is essentially invariant with laser power and temperature, the G-band position decreases significantly (by almost 20 cm^{-1}) from 0.05 to 6 mW, an equivalent reduction in band position on heating to 500 ˚C. The D2 band position decreases slightly with laser power and temperature to approximately 300˚C, but then shifts back towards higher wavenumber with both laser power and temperature. Considering the general decrease in G-band position with laser power and temperature in Figure 7a, we conclude that for 458 nm laser excitation, there is roughly 100˚C of equivalent heating per mW of increased laser power between 0.05 and 6 mW. The slope of band position with temperature and laser power is further confirmed by comparison to the high-temperature data of Huang et al. (2010) (Figure 7b).

Although many of the observed spectral changes by laser-induced heating are comparable to bulk-heating the sample at laser powers below the damage threshold, namely, reduction of band intensities, band intensity ratios, and peak positions, some aspects of the spectral evolution of kerogen are different. In particular, on heating to above ~350 °C we observe an abrupt drop in the R1 ratio, which is not observed with laser powers up to 6 mW (Figure 5). Whereas the FWHM of the D2 band increases with both laser power and heating temperature, the FWHM of G and D1 increases before sharpening up above 2 mW while the FWHM of G and D1 increases gradually with bulk sample heating (Figure 6). We do not have an obvious explanation for these

observed differences, requiring further study, but maintain a broad equivalency exists between laser-induced heating and bulk heating based upon the band shifts shown in Figure 7.

To summarize the results of our tests on the influence of laser power on Raman spectra of kerogen, blue-green excitation lasers should not to exceed 1 mW, and preferably spectra should be collected at laser powers less than 0.1 mW. With a focal spot diameter of ~2 μm, 0.1 mW corresponds to a total irradiance of about 3 kW/cm^2. For the purpose of studying the evolution of kerogen Raman spectra with simultaneous pressure and temperature, we used a laser power of 0.05 mW (~1.6 kW/cm^2), as measured focusing through the sapphire of an open cell, ensuring no effects of laser heating.

High-pressure high-temperature Raman spectra of kerogen

The use of a resistively-heated sapphire cell permitted collection of first-order Raman spectra of kerogen as a function of pressure and temperature up to 3.2 GPa and 380 °C. In the current configuration, achieving pressures >3.2 GPa while heating to above 400 °C was not possible, and several anvil breakages occurred. Future experiments with different gasket materials and/or culets smaller than 300 μm should allow for higher P-T conditions to be reached.

We measured first-order Raman spectra of kerogen at around 80 different pressure-temperature points between 0-3.2 GPa and 25-380 °C. Representative spectra are shown in Figure 8a as a function of pressure at room temperature, and in Figure 8b at simultaneous high pressures and temperatures. We observe no significant change or breakdown of kerogen over the experimental P-T range.

Kerogen spectra taken in the sapphire cell as a function of pressure up to 3.2 GPa at room temperature are shown in Figure 8a, illustrating very little change of no more than 10 cm^{-1} shift in the position of the G+D2 band, but a small shift of ~20 cm^{-1} to higher wavenumbers of the D1 band position. Figure 8b shows spectra recorded at simultaneous P-T conditions up to 3.2 GPa and 380 ˚C, also showing no major changes in the bonding configuration of kerogen. To systematically assess the influence of pressure and temperature on band positions, Figure 9 shows the evolution D1, D2, and G band positions from all P-T conditions visited during this study. We separated each plot to show data at high temperatures but various pressures (Figure 9a,c,e), and separately as a function of pressure at various temperatures (Figure 9b,d,f). For the purpose of analyzing the effect of pressure on the temperature evolution of the bands, we fitted the high-temperature variability of band positions at all pressures above 0.8 GPa (Figure 9).

Pressure cycling

To test the reversibility in the shift of G, D1, and D2 bands with pressure over the current experimental pressure range, we performed a pressure cycling experiment where the initial spectrum was taken at room pressure in the sapphire cell, loaded to 3.1 GPa, and allowed to rest for 72 hours, during which time the pressure increased marginally to 3.3 GPa. The cell was then brought back to room pressure for re-measurement. Figure 10a demonstrates complete reversibility in the kerogen spectra up to 3.3 GPa at room temperature. This is in contrast to pressurization to 9 GPa by Huang et al. (2010), who observed reversibility in the G, D1, and D2 band positions, but the sample recovered from 9 GPa had considerably less intensity and broader peak widths.

Heating-cooling cycles

One of the surprising results of Huang et al. (2010) was the observed reversibility in shift with temperature of D1, D2, and G band positions; being fully recoverable up to 600 ˚C. We measured the D1, D2, and G band positions along a cycling heating path up to the instantaneous breakdown observed at temperatures around 500 ˚C. Figure 11 shows the D1, D2, and G band position on heating to 200, 300, 400, and 450 ˚C, as well as band positions at room temperature between each subsequent thermal maximum. In the D1 band (Figure 11a), spectra taken while at high temperature show a shift toward lower peak position wavenumbers with increasing temperature, as also shown by (Huang et al. 2010). Room temperature D1 band spectra taken between each high temperature measurement have peak positions shifted higher than the original room temperature measurement, and shift higher following each successive heating. The D1 band represents the A_{1g} breathing vibration mode of aromatic rings (Ferrari and Robertson 2000; Beyssac et al. 2003b) and the shift to lower frequencies of D1 at high temperature is the result of softening of the C-C bond strength (Raravikar et al. 2002). The shift toward higher D1 band position at room temperature following each high temperature measurement is the result of catagenic thermal degradation of non-aromatic structures (Vandenbroucke and Largeau 2007) and the prevalence of smaller aromatic clusters, which are known to shift the D1 band higher (Ferrari and Robertson 2000). The D2 and G bands both represent the E2g-derived stretching mode (e.g Marshall et al. 2009). Similar trends with sequential heating and cooling are seen in the D2 and G band position through 400 ˚C, after which the bands shift towards each other as the sample moves toward graphitization, potentially signifying destruction of bonds at sp^2 sites (Ferrari and Robertson 2000).

Temperature cycling also shows irrecoverable changes in the R1 and R2 ratios. Figure 12 shows R1 and R2 as a function of temperature before and after heating to 200, 300, 400, and 450 ˚C, while holding temperature for 10 minutes. The irrecoverable changes in R1 and R2 show the loss of signal intensity with thermal degradation, which more degradation attributable to the D1 band in R1 and both defect bands in R2. At temperatures above 450 ˚C under Ar-gas flow, open-cell heating of kerogen results in major degradation of the sample, similar to that seen by Tissot et al. (1974). This is indicated in Raman spectra by a loss of signal intensity and the sample is visually altered, becoming lighter in color before degradation. The reversibility in D1, D2, and G band frequency following heating to 600 °C in Huang et al. (2010) is within 10 cm^{-1}, which is comparable to the total change observed in our temperature-cycling experiments (Figure 11). In both studies, band intensities do not recover from heating experiments. In addition, there are likely differences owing to the fact that the sample from Huang et al. (2010) may have a different depositional history and subsequent geologic thermal maturation pathway.

To examine the reversibility of peak intensity and position after longer heating durations at high pressure, we performed several continuous heating experiments on the same sample, each lasting between 2-8 hours. The same sample was heated to 450 ˚C at 2.7-3.0 GPa and held for 4, 8, 5, 5, and 2 hours, with recovery to room temperature in between each heating experiment. As an example, a spectrum collected at 450 ˚C and ~2.7 GPa is shown in Figure 10b before and after heating for five hours. Whereas we observed instantaneous and irreversible changes in the Raman spectra collected above ~350 ˚C at room pressure (Figures 3, 5), the spectra recovered from 450 ˚C and ~3 GPa from long-duration heating experiments is completely reversible (Figure 10b), indicating that pressure effectively stabilizes the isolated kerogen to higher temperatures.

DISCUSSION

The use of laser power in the blue-green region greater than 0.1 mW (3 kW/cm^2) has the potential to alter the integrity of kerogen samples by simulating natural thermal maturity/metamorphic grade. Evidence for this comes from irreversible loss of intensity in all peaks with increasing laser power, particularly the loss of intensity in the D1, D2, and G bands, considered indicative of natural thermal maturity/metamorphic grade (Figure 4a). Direct thermal alteration by heating reveals decreases in the intensity of these bands as well, and suggests that laser heating is able to simulate natural thermal maturity.

The laser degradation of CM analogues to natural thermal maturity/metamorphic grade is also indicated by several other diagnostic band parameters. Decreases in area of the D1 and D3 band are considered indicative of natural thermal maturity, however similar results are seen with laser induced heating of the sample (Figure 13). Decreased intensity of the D1 and D2 peaks is also considered indicative of natural thermal maturity, and laser induced heating resulted in a similar decrease (Figure 4). Shifts to lower wavenumber of the G band are also used to indicated natural thermal maturity, however laser induced heating of the sample was able to produce this effect as well (Figure 7).

Direct heating experiments in this study were compared with results from other kerogen heating experiments. The peak position of the D1, D2, and G bands shows good correlation between data of this experiment and that reported by Huang et al. (2010) (Figure 7). Similar trends of each band, with slightly offset values for each band are likely the result of differences between provenance of sample as well as the laser wavelength. Comparison of laser induced band shifts with direct heating and heating results of Huang et al. (2010) suggests that laser induced heating can cause shifts in band position similar to large natural thermal maturity ranges

(Figure. 7). Laser power as low as 1 mW can allow the interpretation that the sample has experienced thermal alteration to 100 °C. At laser powers of 6 mW, sample peak position is comparable to temperatures greater than 500 °C.

Previous studies interpreting kerogen Raman bands for assessment of thermal maturity have used laser power at the sample of greater than 1 mW, and as high as 15 mW (e.g. Pasteris and Wopenka 1991; Wopenka and Pasteris 1993; Beyssac et al. 2002a, 2002b; Huang et al. 2010), although the wavelength of the excitation laser needs to be taken into consideration of damage thresholds. The absorption coefficient of typical type-II kerogen, for example, is about 20% less at 532 nm compared with 458 nm (Ferralis et al. 2015). We found at 458 nm, the use of laser power greater than even 0.1 mW has the potential to induce thermal alteration to kerogen samples, thus complicating the interpretation of bands for thermal maturity.

Huang et al. (2010) measured first-order Raman spectra of kerogen between 25-600 ˚C at room pressure, and up to 9 GPa at room temperature, finding that in general, the stretching frequency (ν, in cm^{-1}) of major bands (D1, D2, and G) decreases with increasing temperature and increases with increasing pressure. These structural changes signify softening of the mode frequencies with temperature and stiffening of the mode frequencies with pressure, as expected. Huang et al. (2010) reported that the D1, D2, and G band positions decrease in frequency shift with temperature (dv/dT) by -0.020(5), -0.029(6), and -0.025(6) cm^{-1}/°C, respectively. On compression at room temperature, D1, D2, and G band positions increase in frequency shift with pressure (dv/dP) by 5.15, 3.34, and 3.66 cm^{-1}/GPa, respectively. Here we examine the net influence of pressure and temperature on mode-frequency shifts.

Figure 9 shows the D1, D2, and G-band frequencies (in Raman shift, cm^{-1}) as a function of simultaneous pressure and temperature. To display these trends, we plotted data as a function of temperature at various pressures between 0-3.5 GPa in the upper panels of Figure 9, and data as a function of pressure at various temperatures between 20-400 ˚C in the lower panels. We performed error-weighted, linear fits to the band positions as a function of temperature at all pressures above 0.8 GPa, finding -0.017(4), -0.023(3), and -0.027(4) cm^{-1}/°C for the D1, D2, and G bands, respectively. These shifts are comparable within error to those found at room pressure by Huang et al. (2010), with dv/dT = -0.020(5), -0.029(6), and -0.025(6) cm^{-1}/°C for D1, D2, and G, respectively. However, the slight reduction in shift of vibrational frequencies of the disordered carbon modes with temperature (dv/dT) at pressures >1 GPa further indicates that pressure acts to increase the thermal stability of kerogen. We find no dependence of R2 on temperature at room pressure or high pressure up to 450 °C (Figures 5 and 14). However, at room pressure, the R1 value drops sharply (from about 0.8 to 0.3) above ~350 °C (Figure 5b), indicating a significant change in the kerogen structure. However, at high pressures (>0.8 GPa), the R1 value is invariant up to nearly 400 ˚C (Figure 14a), indicating that pressure acts to stabilize disordered kerogen at high temperatures. In contrast to heating at room pressure, where the R1 and R2 ratios decrease with increasing temperature (Figure 9), at high pressures (>1 GPa) there is no discernable variation in R1 and R2 as a function of temperature up to 380 °C.

IMPLICATIONS

Kerogen, broadly defined as insoluble macromolecular organic matter (OM), is considered the most abundant form of OM on Earth (Vandenbroucke and Largeau 2007). In addition to being the source material of oil and natural gas, fossil kerogen passing through the oil

window in subduction zones along active margins becomes part of the global carbon cycle. Understanding the evolution of kerogen structure and stability at high pressures and temperatures will therefore illuminate the interface between surface and mantle carbon (diamond). Our experiments suggest that pressures of just a few GPa raises the temperature at which bonds begin to cleave in kerogen to over 450 ˚C.

Figure 15 illustrates the pressure-temperature points visited in this study in comparison to several slab geotherm models. The survival of kerogen to pressures above 3 GPa and 450 ˚C indicates that a significant fraction of kerogen in marine sediments may survive deeper into the subduction zone and uppermost mantle. If modern marine sediment subduction along all convergent boundaries is equal to 0.2 Tmol OC yr^{-1} (Hayes and Waldbauer 2006), a total mass of 60 Tg OC yr^{-1} could be recycled into the mantle. The total terrestrial organic carbon burial flux to the oceans of 58±17 Tg yr^{-1} (Burdige 2005) is disproportionately contributed by convergent margins due to high burial efficiencies (Blair and Aller 2012). In these convergent margin systems 10 – 75% of the buried terrestrial organic carbon is kerogen, resulting in ~2.5 – 45 Tg yr^{-1} of kerogen burial. Therefore ~4 to 75% of organic carbon subducted could be kerogen. The presence of carbonate melts deeper in the mantle eventually leads to diamond formation, and some diamonds indicate a significant fraction of organic source carbon, with light $\delta^{13}C$ values of less than -10‰, and ranging as low as -24‰. (Walter et al. 2011) Kerogen isotope values typically range from approximately -20 to -30‰ (Galimov 1980; Whiticar 1996).

Interpretation of kerogen Raman spectra requires care because of the very high sensitivity of kerogen to laser heating by blue-green excitation wavelengths. We observed irreversible changes in the band positions and ratios at laser powers for 458 nm above about 1 mW, and recommend laser power, as measured at the sample, to be below 0.1 mW for tightly-focused,

confocal measurements of kerogen in the blue-green region. The Raman Laser Spectrometer (RLS) for the ExoMars 2018 rover mission produces a spot size of 50 μm diameter, and the output intensity has been fixed with an upper limit to produce a total irradiance of 0.8-1.2 kW/cm^2 (Rull et al. 2013). The upper limit of the ExoMars-RLS was set specifically to remain below the threshold of thermal damage to powder grains of oxides, hydroxides, and potential organics. Although the ExoMars RLS uses a slightly longer wavelength (532 nm versus 458 nm in this study), a rough comparison can be made. We conservatively put the damage threshold for 458 nm at 0.05-1.0 mW, and conducted most of our experiments at 0.05 mW. For our approximate beam focus diameter of 2 microns (nearly diffraction limited), using a power of 0.05 mW corresponds to a total irradiance of about 1.6 kW/cm^2, which is just above the current irradiance limit set on the ExoMars RLS at 1.2 kW/cm^2 (Rull et al. 2013). Because the absorbance of kerogen decreases roughly 20% between 458 and 532 nm (Ferralis et al. 2015), the damage threshold we found for 458 nm (above ~3 kW/cm^2) could be conservatively reduced to about 2.4 kW/cm^2 for a 532 nm laser. We therefore confirm the ExoMars-RLS laser output has been set to an appropriate limit for the investigation of potential carbonaceous material on Mars.

ACKNOWLEDGMENTS

This research was supported in part by NSF grant EAR-1452344, the David and Lucile Packard Foundation, and the Carnegie DOE Alliance Center to SDJ. LBC was supported in part by a Schlanger Scientific Ocean Drilling Fellowship and by NSF award OCE-1144483 to Neal Blair at Northwestern University. We thank M. Siqueira at Almax-easyLab for discussions about fabrication of custom sapphire-anvils and W.A. Bassett for help with construction of the high-temperature sapphire cell.

REFERENCES

Ammar, M.R., Charon, E., Rouzaud, J.-N., Aleon, J., Guimbretière, G., and Simon, P. (2011) On a Reliable Structural Characterization of Polished Carbons in Meteorites by Raman Microspectroscopy. Spectroscopy Letters, 44, 535–538.

Beny-Bassez, C., and Rouzaud, J.-N. (1985) Characterization of carbonaceous materials by correlated electron and optical microscopy and raman microspectroscopy. Scanning Electron Microscopy, 1, 119–132.

Beyssac, O., Rouzaud, J.-N., Goffé, B., Brunet, F., and Chopin, C. (2002a) Graphitization in a high-pressure, low-temperature metamorphic gradient: a Raman microspectroscopy and HRTEM study. Contributions to Mineralogy and Petrology, 143, 19–31.

Beyssac, O., Goffé, B., Chopin, C., and Rouzaud, J.-N. (2002b) Raman spectra of carbonaceous material in metasediments: A new geothermometer. Journal of Metamorphic Geology, 20, 859–871.

Beyssac, O., Brunet, F., Petitet, J.-P., Goffé, B., and Rouzaud, J.-N. (2003a) Experimental study of the microtextural and structural transformations of carbonaceous materials under pressure and temperature. European Journal of Mineralogy, 15, 937–951.

Beyssac, O., Goffé, B., Petitet, J.-P., Froigneux, E., Moreau, M., and Rouzaud, J.-N. (2003b) On the characterization of disordered and heterogeneous carbonaceous materials by Raman spectroscopy. Spectrochimica Acta - Part A: Molecular and Biomolecular Spectroscopy, 59, 2267–2276.

Blair, N.E., and Aller, R.C. (2012) The Fate of Terrestrial Organic Carbon in the Marine Environment. Annual Review of Marine Science, 4, 401–423.

Blair, N.E., Leithold, E.L., Ford, S.T., Peeler, K.A., Holmes, J.C., and Perkey, D.W. (2003) The

488 persistence of memory: The fate of ancient sedimentary organic carbon in a modern
489 sedimentary system. Geochimica et Cosmochimica Acta, 67, 63–73.
490 Blair, N.E., Leithold, E.L., and Aller, R.C. (2004) From bedrock to burial: The evolution of
491 particulate organic carbon across coupled watershed-continental margin systems. Marine
492 Chemistry, 92, 141–156.
493 Blair, N.E., Leithold, E.L., Brackley, H., Trustrum, N., Page, M., and Childress, L. (2010)
494 Terrestrial sources and export of particulate organic carbon in the Waipaoa sedimentary
495 system: Problems, progress and processes. Marine Geology, 270, 108–118.
496 Bonal, L., Quirico, E., Bourot-Denise, M., and Montagnac, G. (2006) Determination of the
497 petrologic type of CV3 chondrites by Raman spectroscopy of included organic matter.
498 Geochimica et Cosmochimica Acta, 70, 1849–1863.
499 Bouchez, J., Beyssac, O., Galy, V., Gaillardet, J., France-Lanord, C., Maurice, L., and Moreira-
500 Turcq, P. (2010) Oxidation of petrogenic organic carbon in the Amazon floodplain as a
501 source of atmospheric CO2. Geology, 38, 255–258.
502 Burdige, D.J. (2005) Burial of terrestrial organic matter in marine sediments: A re-assessment.
503 Global Biogeochemical Cycles, 19, 1–7.
504 Busemann, H., Alexander, C.M.O., and Nittler, L.R. (2007) Characterization of insoluble organic
505 matter in primitive meteorites by microRaman spectroscopy. Meteoritics & Planetary
506 Science, 1416, 1387–1416.
507 Courrèges-Lacoste, G.B., Ahlers, B., and Pérez, F.R. (2007) Combined Raman
508 spectrometer/laser-induced breakdown spectrometer for the next ESA mission to Mars.
509 Spectrochimica Acta - Part A: Molecular and Biomolecular Spectroscopy, 68, 1023–1028.
510 Czaja, A.D., Kudryavtsev, A.B., Cody, G.D., and Schopf, J.W. (2009) Characterization of

permineralized kerogen from an Eocene fossil fern. Organic Geochemistry, 40, 353–364.

Dartnell, L.R., Page, K., Jorge-Villar, S.E., Wright, G., Munshi, T., Scowen, I.J., Ward, J.M., and Edwards, H.G.M. (2012) Destruction of Raman biosignatures by ionising radiation and the implications for life detection on Mars. Analytical and bioanalytical chemistry, 403, 131–44.

Drenzek, N.J., Hughen, K.A., Montluçon, D.B., Southon, J.R., dos Santos, G.M., Druffel, E.R.M., Giosan, L., and Eglinton, T.I. (2009) A new look at old carbon in active margin sediments. Geology, 37, 239–242.

Dunn, D.S., Sridhar, N., Miller, M.A., Price, K.T., Pabalan, R., and Abrajano, T.A. (2007) Development of a surface-enhanced Raman technique for biomarker studies on mars. Applied Spectroscopy, 61, 25–31.

Durand, B. (1980) Sedimentary organic matter and kerogen. Definition and quantitative importance of kerogen. In B. Durand, Ed., Kerogen, Insoluble Organic Matter from Sedimentary Rocks pp. 13–34. Editions Technip, Paris, France.

Durand, B., and Nicaise, G. (1980) Procedures for kerogen isolation. In B. Durand, Ed., Kerogen, Insoluble Organic Matter from Sedimentary Rocks pp. 35–54. Editions Technip, Paris, France.

Ellery, A., Wynn-Williams, D., Parnell, J., Edwards, H.G.M., and Dickensheets, D. (2004) The role of Raman spectroscopy as an astrobiological tool in the exploration of Mars. Journal of Raman Spectroscopy, 35, 441–457.

Everall, N., Lumsdon, J., and Christopher, D. (1991) The effect of laser-induced heating upon the vibrational raman spectra of graphites and carbon fibres. Carbon, 29, 133–137.

Ferralis, N., Liu, Y., Bake, K.D., Pomerantz, A.E., and Grossman, J.C. (2015) Direct correlation

between aromatization of carbon-rich organic matter and its visible electronic absorption edge. Carbon, 88, 139–147.

Ferrari, A., and Robertson, J. (2000) Interpretation of Raman spectra of disordered and amorphous carbon. Physical Review B, 61, 14095–14107.

Galimov, E.M. (1980) C13/C12 in kerogen. In B. Durand, Ed., Kerogen, Insoluble Organic Matter from Sedimentary Rocks pp. 271–300. Editions Technip, Paris, France.

Galy, V., France-Lanord, C., Beyssac, O., Faure, P., Kudrass, H., and Palhol, F. (2007) Efficient organic carbon burial in the Bengal fan sustained by the Himalayan erosional system. Nature, 450, 407–410.

Galy, V., Beyssac, O., France-Lanord, C., and Eglinton, T. (2008) Recycling of graphite during Himalayan erosion: a geological stabilization of carbon in the crust. Science (New York, N.Y.), 322, 943–945.

Hayes, J.M., and Waldbauer, J.R. (2006) The carbon cycle and associated redox processes through time. Philosophical transactions of the Royal Society of London, 361, 931–950.

Hilton, R.G., Galy, A., Hovius, N., Horng, M.J., and Chen, H. (2010) The isotopic composition of particulate organic carbon in mountain rivers of Taiwan. Geochimica et Cosmochimica Acta, 74, 3164–3181.

Hochleitner, R., Tarcea, N., Simon, G., Kiefer, W., and Popp, J. (2004) Micro-Raman spectroscopy: A valuable tool for the investigation of extraterrestrial material. Journal of Raman Spectroscopy, 35, 515–518.

Huang, E.-P.E., Huang, E.-P.E., Yu, S.-C., Chen, Y.-H., Lee, J.-S., and Fang, J.-N. (2010) In situ Raman spectroscopy on kerogen at high temperatures and high pressures. Physics and Chemistry of Minerals, 37, 593–600.

557 Hutchinson, I.B., Parnell, J., Edwards, H.G.M., Jehlicka, J., Marshall, C.P., Harris, L. V, and
558 Ingley, R. (2014) Potential for analysis of carbonaceous matter on Mars using Raman
559 spectroscopy. Planetary and Space Science, 103, 184–190.
560 Kagi, H., Tsuchida, I., Wakatsuki, M., Takahashi, K., Kamimura, N., Iuchi, K., and Wada, H.
561 (1994) Proper understanding of down-shifted Raman spectra of natural graphite: Direct
562 estimation of laser-induced rise in sample temperature. Geochimica et Cosmochimica Acta,
563 58, 3527–3530.
564 Kelemen, S.R., and Fang, H.L. (2001) Maturity trends in Raman spectra from kerogen and coal.
565 Energy and Fuels, 15, 653–658.
566 Kennedy, C.S., and Kennedy, G.C. (1976) The Equilibrium Boundary Between Graphite and
567 Diamond. Journal of Geophysical Research, 81, 2467–2470.
568 Kremer, B., Bauer, M., Stark, R.W., Gast, N., Altermann, W., Gursky, H.-J., Heckl, W.M., and
569 Kazmierczak, J. (2012) Laser-Raman and atomic force microscopy assessment of the
570 chlorococcalean affinity of problematic microfossils. Journal of Raman Spectroscopy, 43,
571 32–39.
572 Lahfid, A., Beyssac, O., Deville, E., Negro, F., Chopin, C., and Goffé, B. (2010) Evolution of the
573 Raman spectrum of carbonaceous material in low-grade metasediments of the Glarus Alps
574 (Switzerland). Terra Nova, 22, 354–360.
575 Leithold, E.L., Blair, N.E., and Perkey, D.W. (2006) Geomorphologic controls on the age of
576 particulate organic carbon from small mountainous and upland rivers. Global
577 Biogeochemical Cycles, 20, 1–11.
578 Mackenzie, F.T., Lerman, A., and Andersson, A.J. (2004) Past and present of sediment and
579 carbon biogeochemical cycling models. Biogeosciences Discussions, 1, 27–85.

580 Marshall, A.O., Corsetti, F.A., Sessions, A.L., and Marshall, C.P. (2009) Raman spectroscopy
581 and biomarker analysis reveal multiple carbon inputs to a Precambrian glacial sediment.
582 Organic Geochemistry, 40, 1115–1123.
583 Matsuda, J., Morishita, K., Tsukamoto, H., Miyakawa, C., Nara, M., Amari, S., Uchiyama, T.,
584 and Takeda, S. (2010) An attempt to characterize phase Q: Noble gas, Raman spectroscopy
585 and transmission electron microscopy in residues prepared from the Allende meteorite.
586 Geochimica et Cosmochimica Acta, 74, 5398–5409.
587 Morishita, K., Nara, M., Amari, S., and Matsuda, J. (2011) On the Effect of Laser-Induced
588 Heating in a Raman Spectroscopic Study of Carbonaceous Material in Meteorite.
589 Spectroscopy Letters, 44, 459–463.
590 Pasteris, J.D., and Wopenka, B. (1991) Raman Spectra of Graphite as Indicators of Degree of
591 Metamorphism. Canadian Mineralogist, 29, 1–9.
592 Pasteris, J.D., and Wopenka, B. (2002) Images of the Earth's earliest fossils? Nature, 420, 476–
593 467.
594 Quirico, E., Raynal, P.-I., and Bourot-Denise, M. (2003) Metamorphic grade of organic matter in
595 six unequilibrated ordinary chondrites. Meteoritics & Planetary Science, 38, 795–811.
596 Rahl, J.M., Anderson, K.M., Brandon, M.T., and Fassoulas, C. (2005) Raman spectroscopic
597 carbonaceous material thermometry of low-grade metamorphic rocks: Calibration and
598 application to tectonic exhumation in Crete, Greece. Earth and Planetary Science Letters,
599 240, 339–354.
600 Raravikar, N., Keblinski, P., Rao, A., Dresselhaus, M., Schadler, L., and Ajayan, P. (2002)
601 Temperature dependence of radial breathing mode Raman frequency of single-walled
602 carbon nanotubes. Physical Review B, 66, 1–9.

603 Rouzaud, J.N., and Oberlin, A. (1989) Structure, microtexture, and optical properties of
604 anthracene and saccharose-based carbons. Carbon, 27, 517–529.
605 Rull, F., Maurice, S., Diaz, E., Lopez, G., Catala, A., and Team, R. (2013) Raman Laser
606 Spectrometer (RLS) for Exomars 2018 Rover Mission: Current status and science operation
607 mode on powdered samples. Lunar and Planetary Science Conference, 1–2.
608 Sadezky, A., Muckenhuber, H., Grothe, H., Niessner, R., and Pöschl, U. (2005) Raman
609 microspectroscopy of soot and related carbonaceous materials: Spectral analysis and
610 structural information. Carbon, 43, 1731–1742.
611 Sandford, S., Aleon, J., Alexander, C., Araki, T., Bajt, S., Baratta, G., Borg, J., Bradley, J.,
612 Brownlee, D., Brucato, J., and others (2006) Organics Captured from Comet 81P/Wild 2 by
613 the Stardust Spacecraft. Science, 314, 1720–1724.
614 Schopf, J.W., and Kudryavtsev, A.B. (2005) Three-dimensional Raman imagery of precambrian
615 microscopic organisms. Geobiology, 3, 1–12.
616 Schopf, J.W., Kudryavtsev, A.B., Agresti, D.G., Wdowiak, T.J., and Czaja, A.D. (2002) Laser-
617 Raman imagery of Earth's earliest fossils. Nature, 3, 73–76.
618 Steele, A., Mccubbin, F.M., Fries, M., Kater, L., Boctor, N.Z., Fogel, M.L., Conrad, P.G.,
619 Glamoclija, M., Spencer, M., Morrow, A.L., and others (2012) A reduced organic carbon
620 component in Martian basalts. Science, 337, 212–215.
621 Syracuse, E.M., van Keken, P.E., and Abers, G.A. (2010) The global range of subduction zone
622 thermal models. Physics of the Earth and Planetary Interiors, 183, 73–90.
623 Tissot, B., Durand, B., Espitalie, J., and Combaz, A. (1974) Influence of nature and diagenesis of
624 organic matter in formation of petroleum. The American Association of Petroleum
625 Geologists Bulletin, 58, 499–506.

626 Tsu, R., Gonzalez, J.H., and Hernandez, I. (1978) Raman scattering in graphite. Bulletin of the
627 American Physical Society, 23, 302–303.
628 Vandenbroucke, M., and Largeau, C. (2007) Kerogen origin, evolution and structure. Organic
629 Geochemistry, 38, 719–833.
630 Wang, Y., Alsmeyer, D.C., and Mccreery, R.L. (1990) Raman Spectroscopy of Carbon
631 Materials: Structural Basis of Observed Spectra. Chemistry of Materials, 2, 557–563.
632 Whiticar, M.J. (1996) Stable isotope geochemistry of coals, humic kerogens and related natural
633 gases. International Journal of Coal Geology, 32, 191–215.
634 Wopenka, B. (1988) Raman observations on individual interplanetary dust particles. Earth and
635 Planetary Science Letters, 88, 221–231.
636 Wopenka, B., and Pasteris, J.D. (1993) Structural characterization of kerogens to granulite-facies
637 graphite: applicability of Raman microprobe spectroscopy. American Mineralogist, 78,
638 533–557.
639
640
641
642
643
644

Figure Captions

Figure 1. First-order (a) and second-order (b) Raman spectra of isolated kerogen from the Eel River, CA, USA. Sum of the deconvolution is shown by the solid black line, with misfit shown below each spectrum. These spectra were collected using 458 nm excitation with 0.05 mW laser power at the sample, collected through a 100x objective (0.7 numerical aperture) for 300 seconds, averaged over three accumulations.

Figure 2. (a) First-order and second-order Raman spectra of kerogen used in this study at various laser power settings measured at the sample position. (b) First-order region detail measured using various laser power settings and plotted with intensity normalized to the G+D2 band.

Figure 3. First-order Raman spectra of kerogen on heating under Ar-gas stream from 22 to 500 ˚C. Dashed grey lines at 1360 cm^{-1} and 1600 cm^{-1} are drawn for reference. Spectra at different temperatures have been shifted for clarity.

Figure 4. Fitted intensity of G, D1, and D2 bands as a function of laser power (a) and temperature (b). In (a), the intensity was normalized to peak intensities measured using 0.05 mW laser power. In (b) all spectra were collected using 0.05 mW laser power and the peak intensities were normalized to the values at 22˚C.

Figure 5. (a) Variation of the R1 and R2 ratios (see text) as a function of laser power. (b) Variation of the R1 and R2 ratios as a function of temperature, measured using 0.05 mW laser

667 power. The abrupt decrease in R1 = $(D1/G)_{Intensity}$ at ~350 °C indicates an increase in the amount
668 of ordered (graphitic) structure.
669
670 Figure 6. Variation of the G, D1, and D2 band widths (FWHM) as a function of laser power (a-c)
671 at room temperature, and as a function of temperature as measured using a laser power of 0.05
672 mW (d-f).
673
674 Figure 7. (a) Variation of the G, D1, and D2 band positions as a function of laser power (solid
675 circles) and as a function of temperature using 0.05 mW laser power (open symbols) from the
676 current study. (b) G, D1, and D2 band positions as a function of laser power (solid symbols)
677 from the current study compared with the effect of temperature from the study of Huang et al.
678 (2010), shown by open symbols.
679
680 Figure 8. First-order Raman spectra of kerogen in a high P-T sapphire cell (a) as a function of
681 pressure up to 3.1 GPa and (b) at various pressures and temperatures up to 3 GPa and 450 ˚C.
682 Spectra at 450 ˚C were collected after 24 hours at 3 GPa and 450 ˚C. Spectra intensity was
683 normalized to a common signal-to-noise ratio. Dashed grey lines for reference are drawn at 1360
684 cm^{-1} and 1620 cm^{-1}.
685
686 Figure 9. Mode frequencies (in Raman shift, cm^{-1}) of the D1 (a,b), D2 (c,d), and G bands (e,f) of
687 kerogen at high pressure and high temperature. In all six panels, data collected at high
688 temperature are shown by pink shaded circles, and data collected at room temperature are shown

by blue shaded squares. Fits to the data as a function of temperature at high pressure (>1.0 GPa) are shown by dashed lines with fits given in the text.

Figure 10. The effect of pressure (a) and high-pressure high-temperature (b) on first-order kerogen Raman spectra are recoverable below 3.3 GPa and 450 ˚C. (a) Shown in black, spectrum measured before compression and in red the spectrum immediately after direct compression to 3.1 GPa. After holding for 72 hours, the pressure increased to 3.3 GPa and was measured again (green). On decompression back to room pressure, the spectrum recovered completely (grey) to its original state. (b) Shown in black, spectrum measured before compression and heating. In red, spectrum taken at 2.7 GPa and 450 °C. Several heating durations of 2-8 hours each were made, with one example shown in green, taken following five continuous hours of heating at 450 °C and 2.7 GPa. Following 24 hours of cumulative heating, the spectrum in grey was obtained at 1.4 GPa and room temperature.

Figure 11. Temperature cycling experiments at room pressure show the positions of D1, D2, and G bands at room temperature (blue shaded squares) prior to and following heating (pink shaded circles) to the temperatures indicated along a heating-cooling thermal sequence.

Figure 12. Temperature cycling experiments at room pressure show irreversible effects of heating on the R1 and R2 ratios at room temperature (blue shaded squares) prior to and following heating (pink shaded circles) to the temperatures indicated along a heating-cooling thermal sequence.

712 Figure 13. Area of disordered D1 and D3 bands as a function of laser power (a) and temperature
713 (b), measured at 0.05 mW laser power at the sample.
714
715 Figure 14. R1 (a,b) and R2 (c,d) ratios of kerogen spectra at high pressure and high temperatures.
716 Data measured at high temperature are shown by pink shaded circles, and data measured at room
717 temperature are shown blue shaded squares. In contrast to heating at room pressure, where the
718 R1 and R2 ratios decrease with increasing temperature (see Figure 9), at high pressures (>1 GPa)
719 there is no discernable variation in R1 and R2 as a function of temperature up to 450 °C.
720
721 Figure 15. Pressure-temperature points visited in the current experiments in comparison to
722 several calculated geotherms in subducted slabs (Syracuse et al. 2010) along oceanic-continental
723 crust. The graphite-diamond phase boundary is shown by the solid black line (Kennedy and
724 Kennedy 1976). The structural integrity of kerogen to the highest P-T condition indicates that
725 instantaneous breakdown of kerogen will not occur in the upper part of slabs, potentially leading
726 to deeper subduction of carbon back into the mantle.
727
728
729
730
731
732
733

734 **Figure 1**

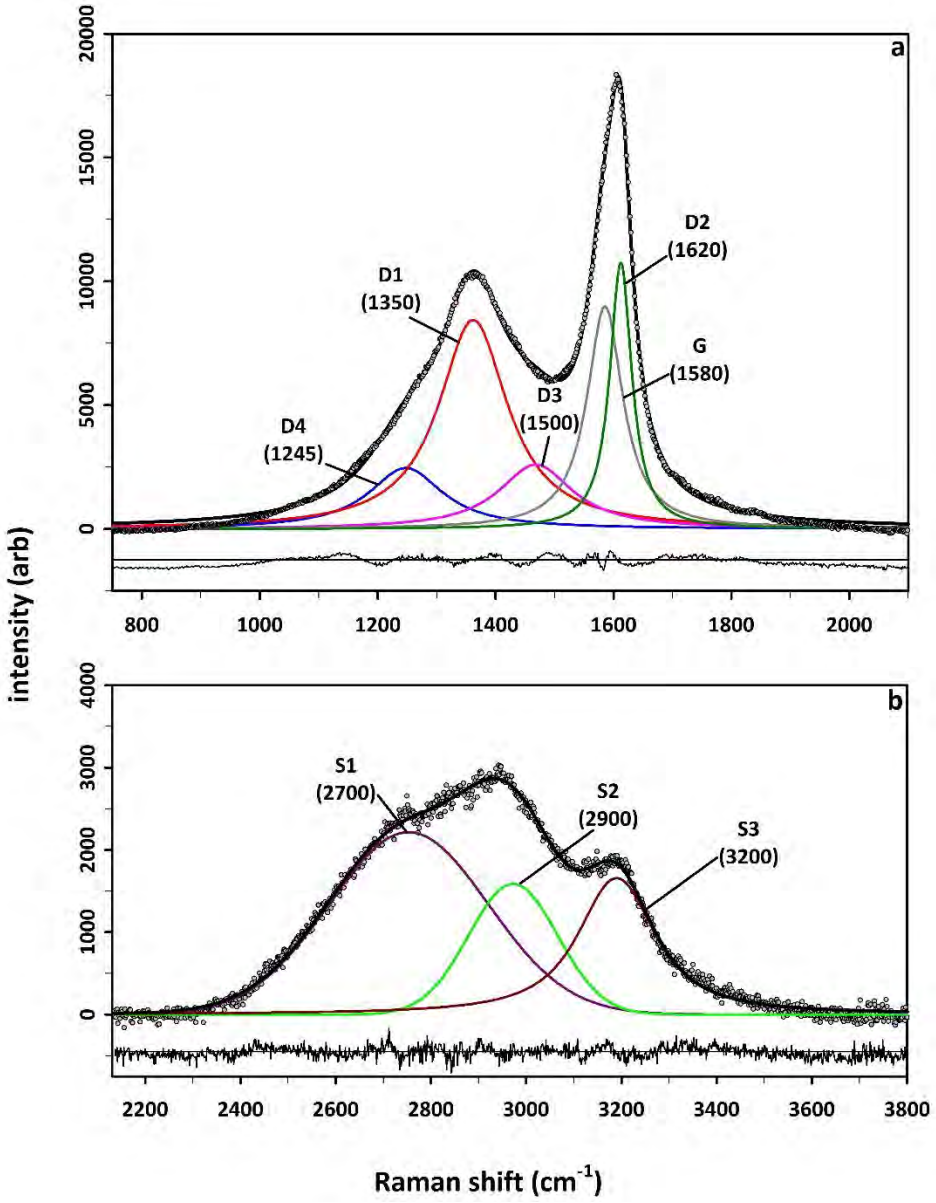

735

736 Figure 1. First-order (a) and second-order (b) Raman spectra of isolated kerogen from the Eel
737 River, CA, USA. Sum of the deconvolution is shown by the solid black line, with misfit shown
738 below each spectrum. These spectra were collected using 458 nm excitation with 0.05 mW laser
739 power at the sample, collected through a 100x objective (0.7 numerical aperture) for 300
740 seconds, averaged over three accumulations.

This is a preprint, the final version is subject to change, of the American Mineralogist (MSA)
Cite as Authors (Year) Title. American Mineralogist, in press.
(DOI will not work until issue is live.) DOI: http://dx.doi.org/10.2138/am-2017-5719

741 **Figure 2**

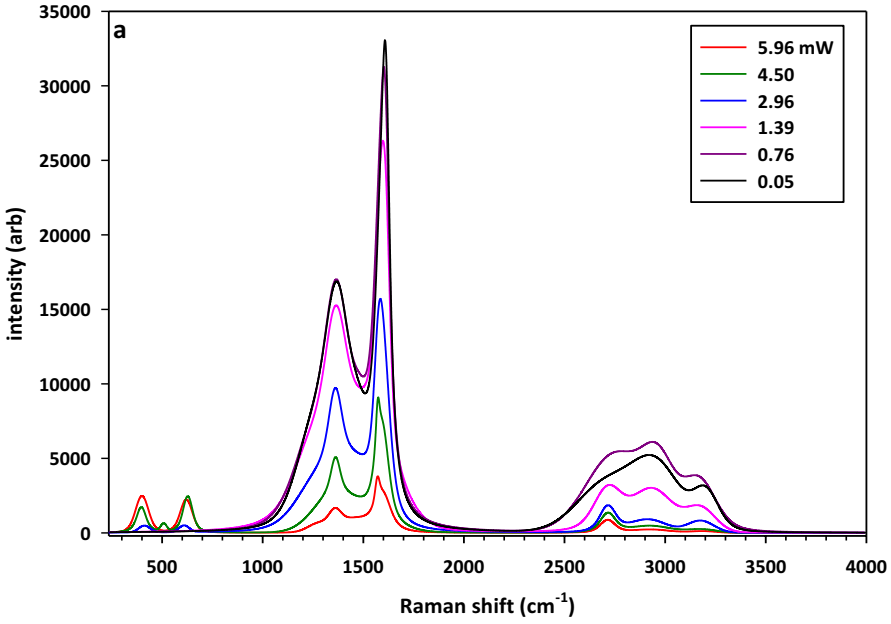

742

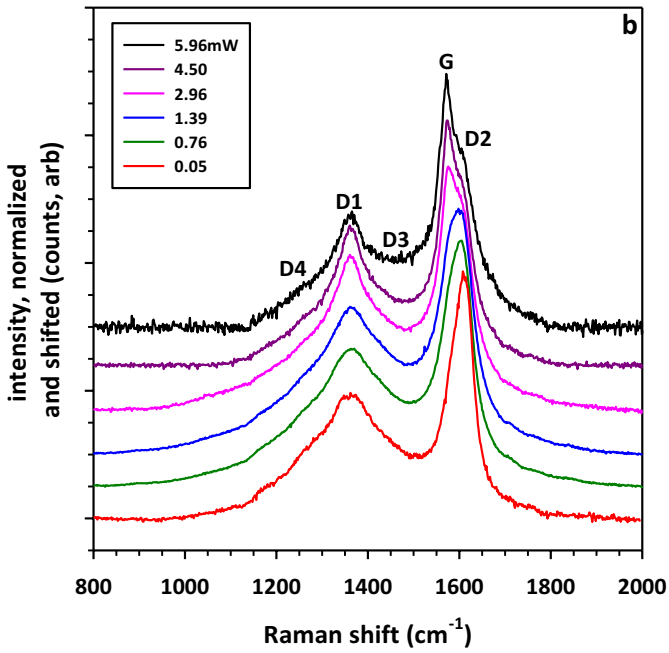

743

744 Figure 2. (a) First-order and second-order Raman spectra of kerogen used in this study at various
745 laser power settings measured at the sample position. (b) First-order region detail measured using
746 various laser power settings and plotted with intensity normalized to the G+D2 band.

747 **Figure 3**

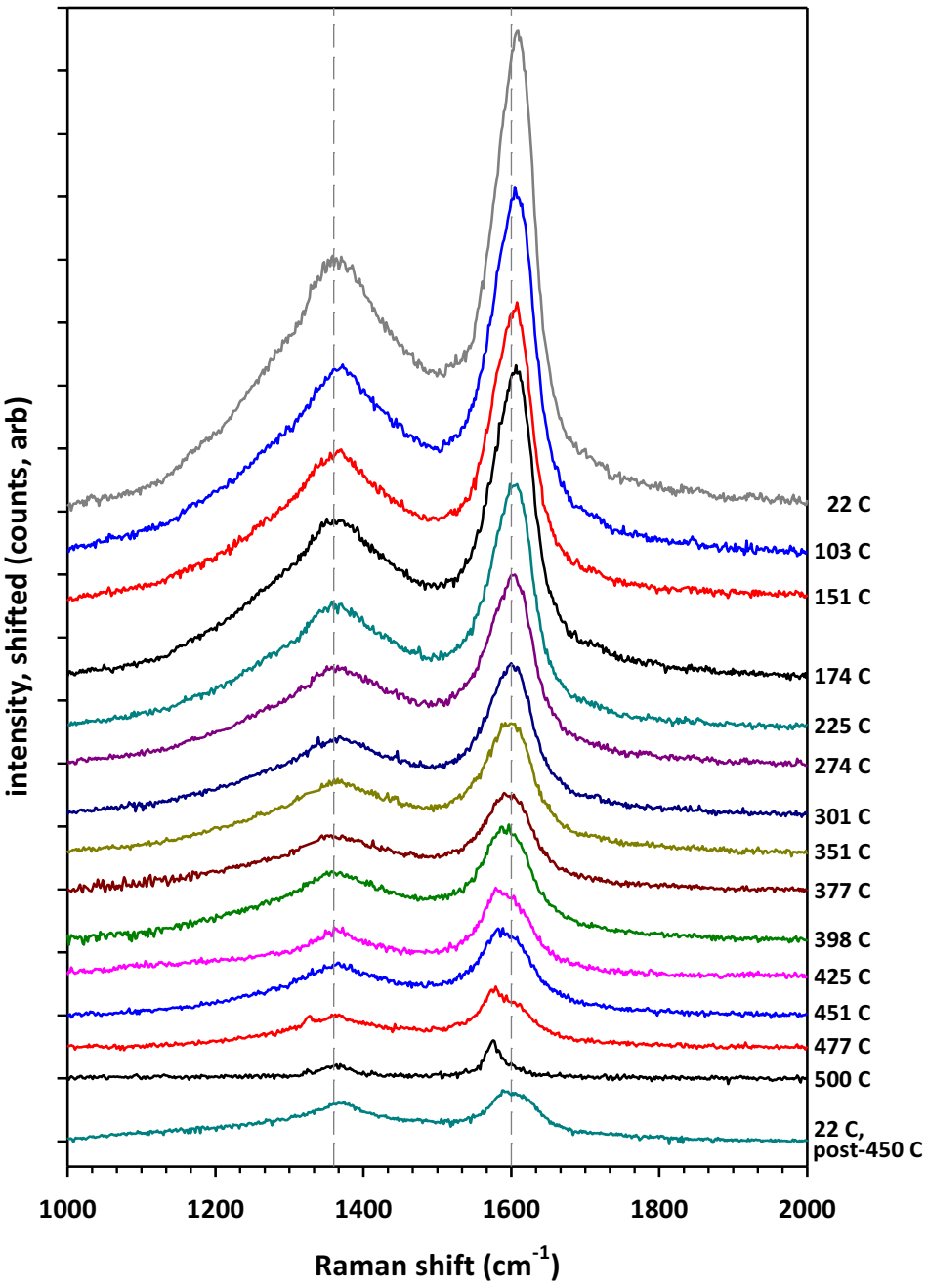

748

749 Figure 3. First-order Raman spectra of kerogen on heating under Ar-gas stream from 22 to 500

750 ˚C. Dashed grey lines at 1360 cm^{-1} and 1600 cm^{-1} are drawn for reference. Spectra at different

751 temperatures have been shifted for clarity.

752

753 **Figure 4**
754

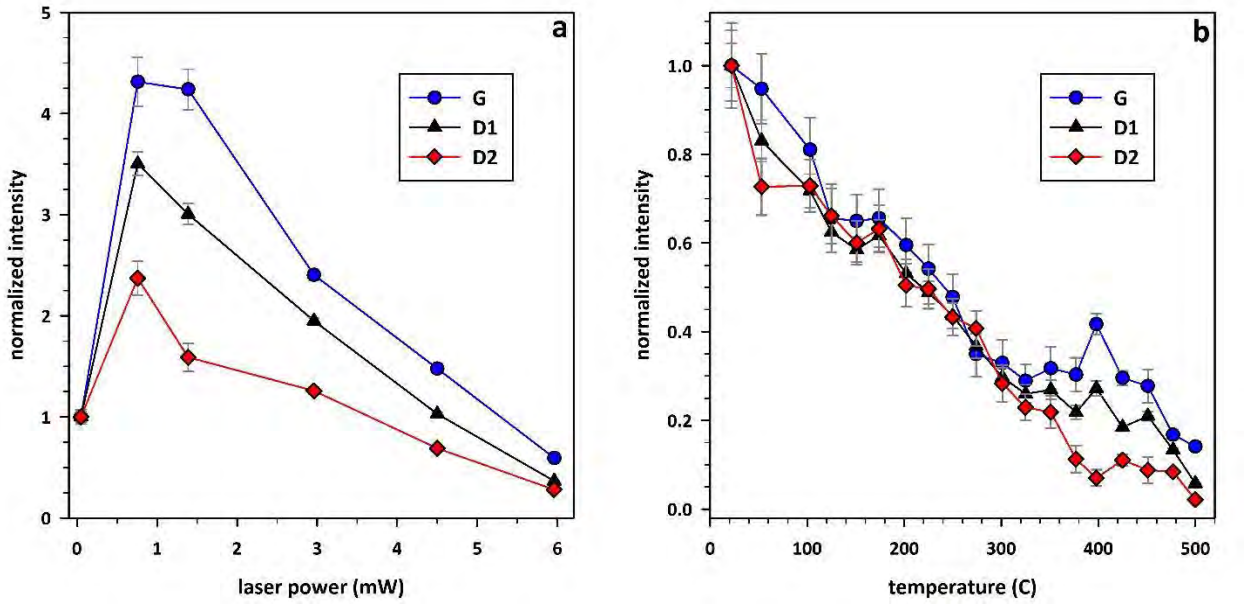

755

756

757 Figure 4. Fitted intensity of G, D1, and D2 bands as a function of laser power (a) and
758 temperature (b). In (a), the intensity was normalized to peak intensities measured using 0.05 mW
759 laser power. In (b) all spectra were collected using 0.05 mW laser power and the peak intensities
760 were normalized to the values at 22˚C.

761

This is a preprint, the final version is subject to change, of the American Mineralogist (MSA)
Cite as Authors (Year) Title. American Mineralogist, in press.
(DOI will not work until issue is live.) DOI: http://dx.doi.org/10.2138/am-2017-5719

762 **Figure 5**

763

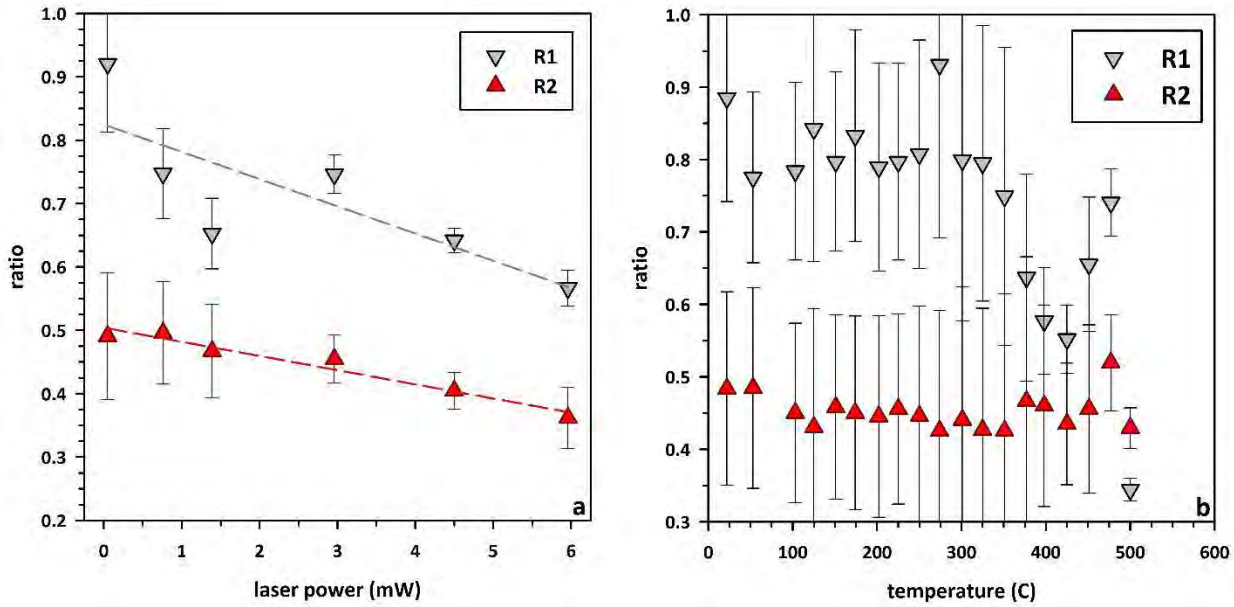

764

765 Figure 5. (a) Variation of the R1 and R2 ratios (see text) as a function of laser power. (b)
766 Variation of the R1 and R2 ratios as a function of temperature, measured using 0.05 mW laser
767 power. The abrupt decrease in R1 = $(D1/G)_{Intensity}$ at ~350 °C indicates an increase in the amount
768 of ordered (graphitic) structure.

769

770 **Figure 6**

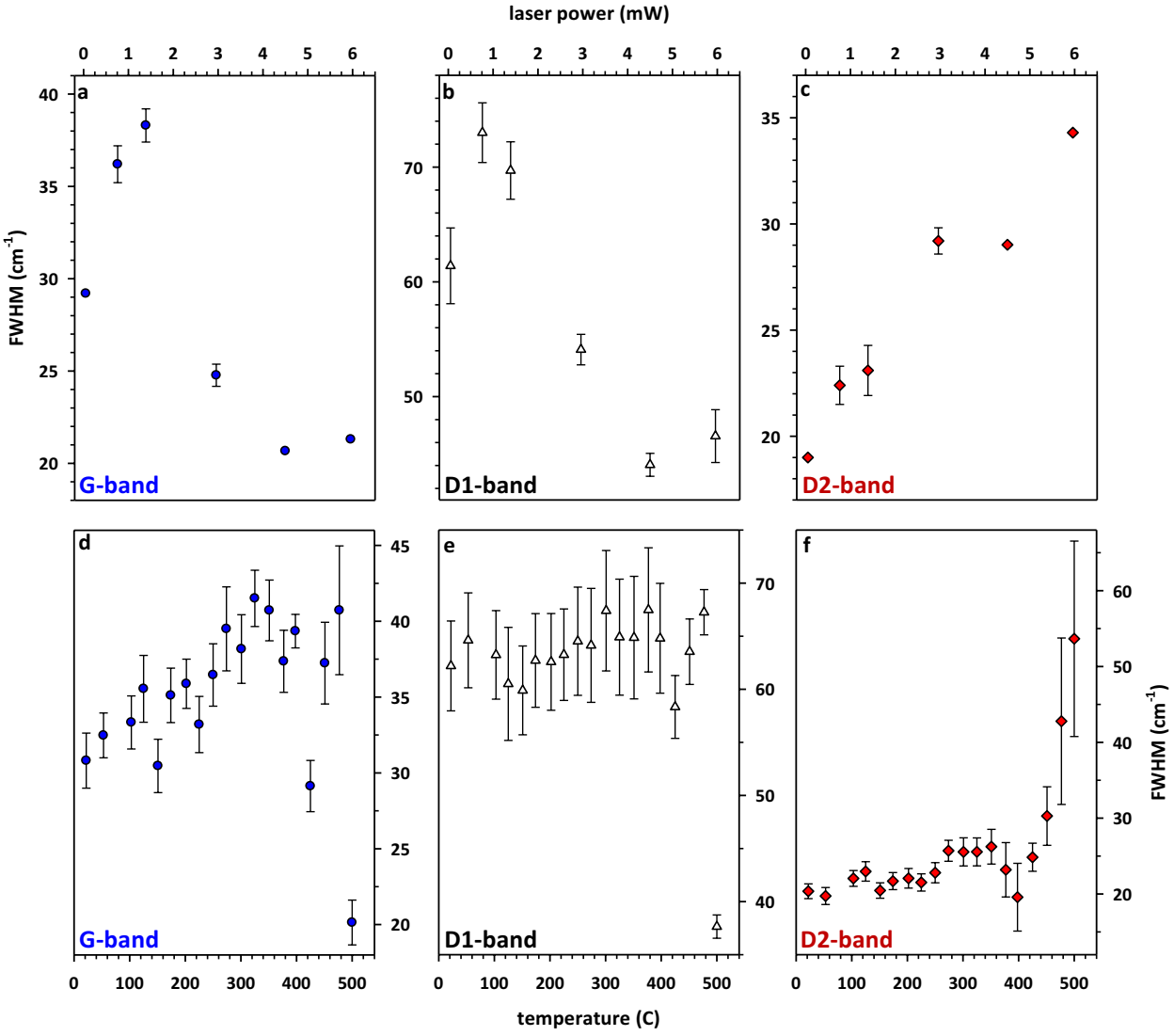

771

772 Figure 6. Variation of the G, D1, and D2 band widths (FWHM) as a function of laser power (a-c)

773 at room temperature, and as a function of temperature as measured using a laser power of 0.05

774 mW (d-f).

775

776 **Figure 7**

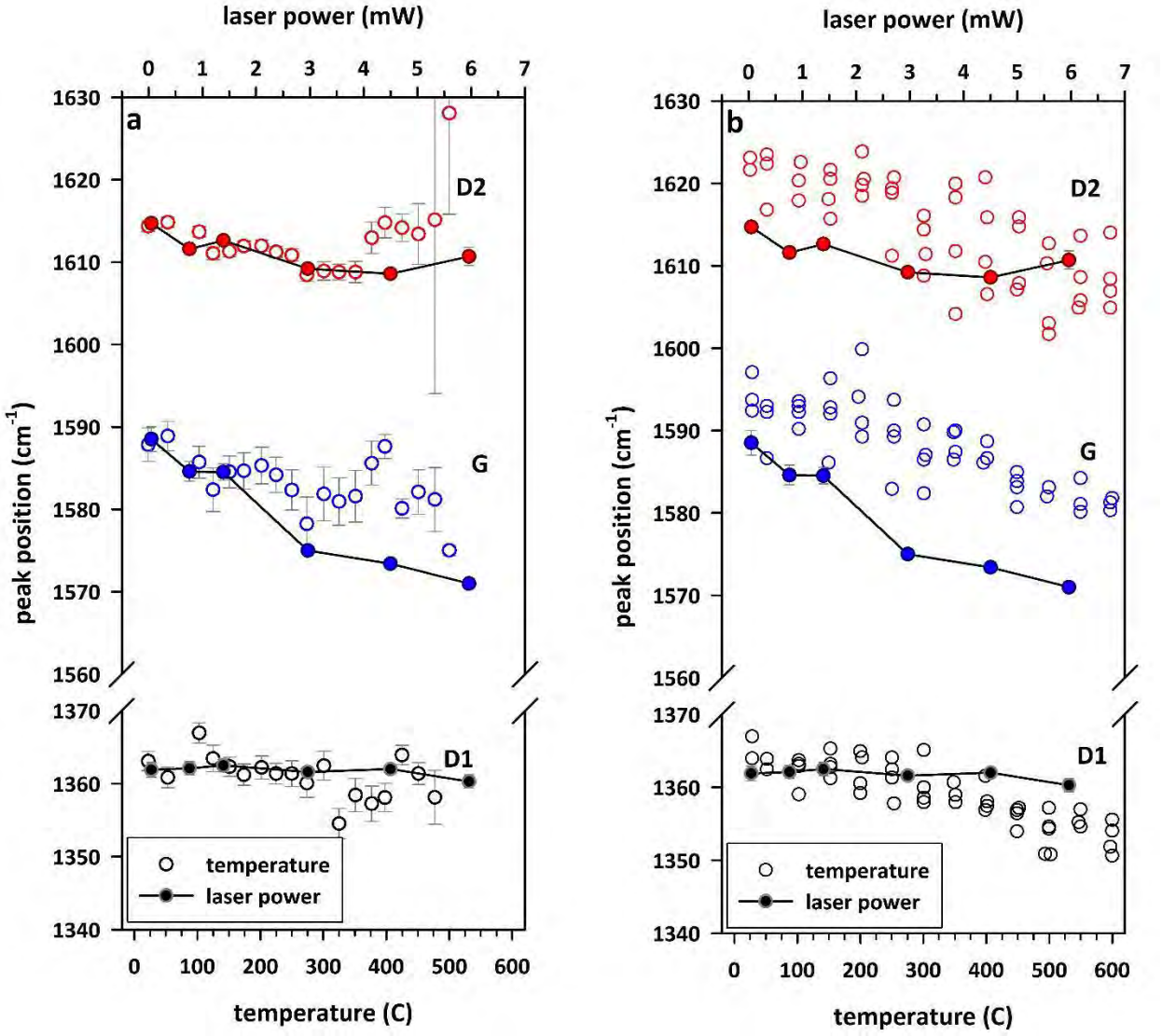

777

778 Figure 7. (a) Variation of the G, D1, and D2 band positions as a function of laser power (solid
779 circles) and as a function of temperature using 0.05 mW laser power (open symbols) from the
780 current study. (b) G, D1, and D2 band positions as a function of laser power (solid symbols)
781 from the current study compared with the effect of temperature from the study of Huang et al.
782 (2010), shown by open symbols.

783

784 **Figure 8**

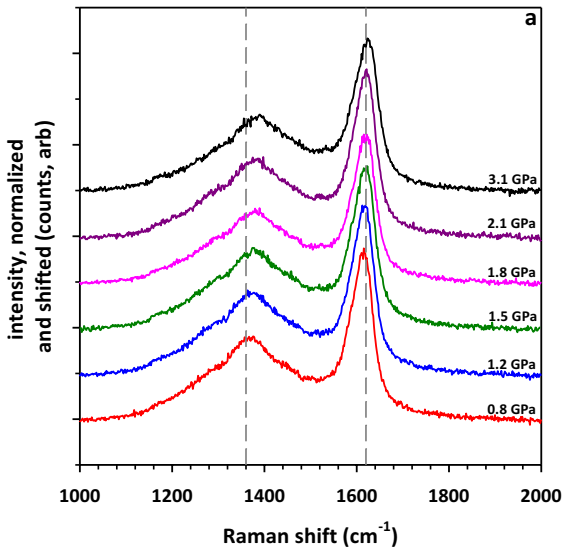

785

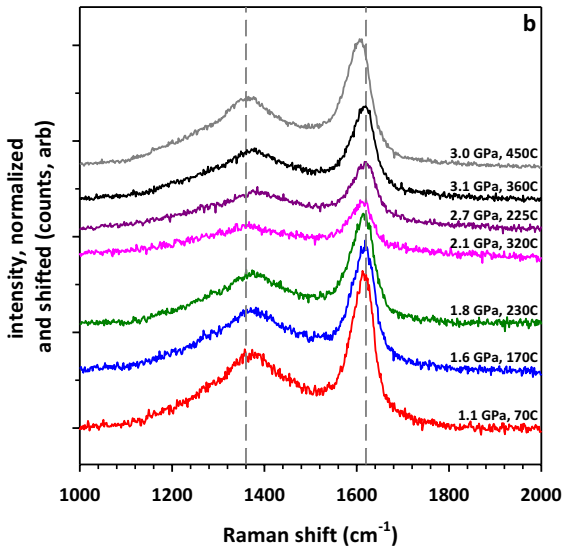

786

787 Figure 8. First-order Raman spectra of kerogen in a high P-T sapphire cell (a) as a function of
788 pressure up to 3.1 GPa and (b) at various pressures and temperatures up to 3 GPa and 450 ˚C.
789 Spectra at 450 ˚C were collected after 24 hours at 3 GPa and 450 ˚C. Spectra intensity was
790 normalized to a common signal-to-noise ratio. Dashed grey lines for reference are drawn at 1360
791 cm^{-1} and 1620 cm^{-1}.

Figure 9

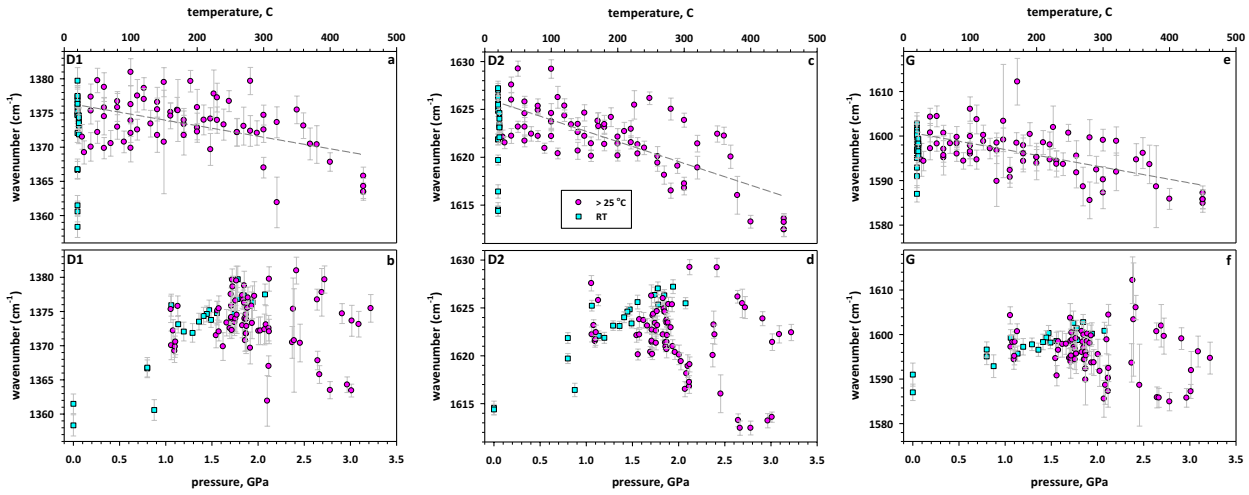

Figure 9. Mode frequencies (in Raman shift, cm^{-1}) of the D1 (a,b), D2 (c,d), and G bands (e,f) of kerogen at high pressure and high temperature. In all six panels, data collected at high temperature are shown by pink shaded circles, and data collected at room temperature are shown by blue shaded squares. Fits to the data as a function of temperature at high pressure (>1.0 GPa) are shown by dashed lines with fits given in the text.

809 **Figure 10**

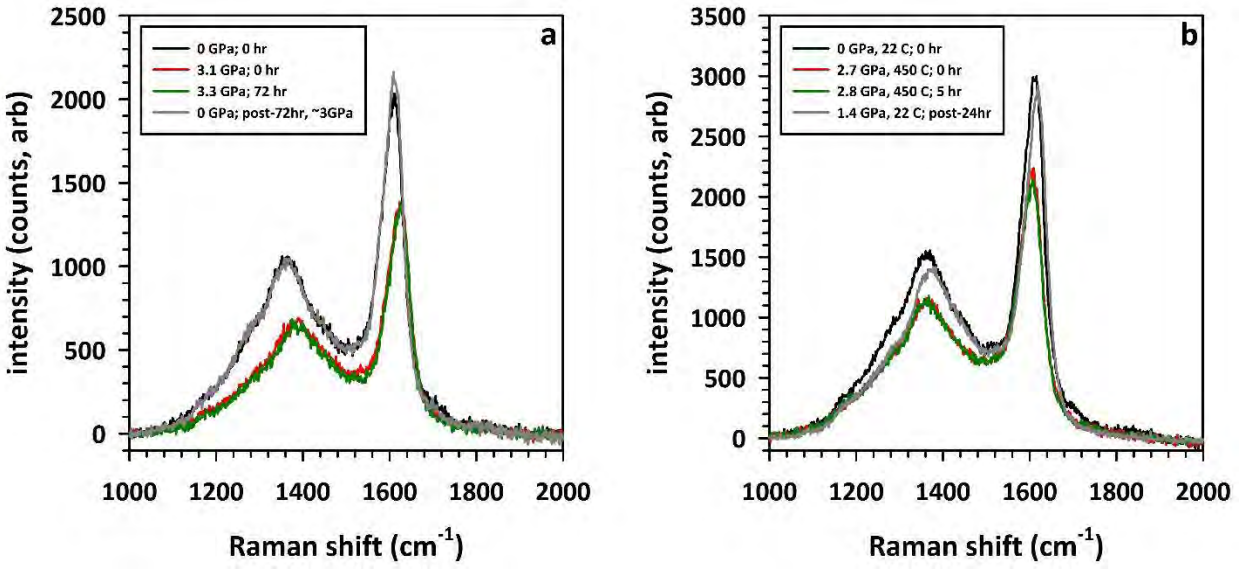

810

811 Figure 10. The effect of pressure (a) and high-pressure high-temperature (b) on first-order
812 kerogen Raman spectra are recoverable below 3.3 GPa and 450 ˚C. (a) Shown in black, spectrum
813 measured before compression and in red the spectrum immediately after direct compression to
814 3.1 GPa. After holding for 72 hours, the pressure increased to 3.3 GPa and was measured again
815 (green). On decompression back to room pressure, the spectrum recovered completely (grey) to
816 its original state. (b) Shown in black, spectrum measured before compression and heating. In red,
817 spectrum taken at 2.7 GPa and 450 °C. Several heating durations of 2-8 hours each were made,
818 with one example shown in green, taken following five continuous hours of heating at 450 °C
819 and 2.7 GPa. Following 24 hours of cumulative heating, the spectrum in grey was obtained at 1.4
820 GPa and room temperature.

821

Figure 11

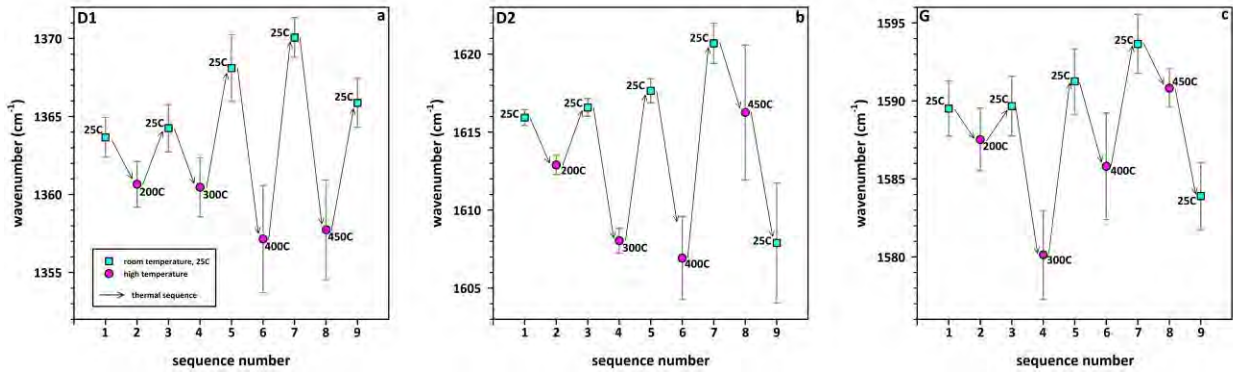

Figure 11. Temperature cycling experiments at room pressure show the positions of D1, D2, and G bands at room temperature (blue shaded squares) prior to and following heating (pink shaded circles) to the temperatures indicated along a heating-cooling thermal sequence.

Figure 12

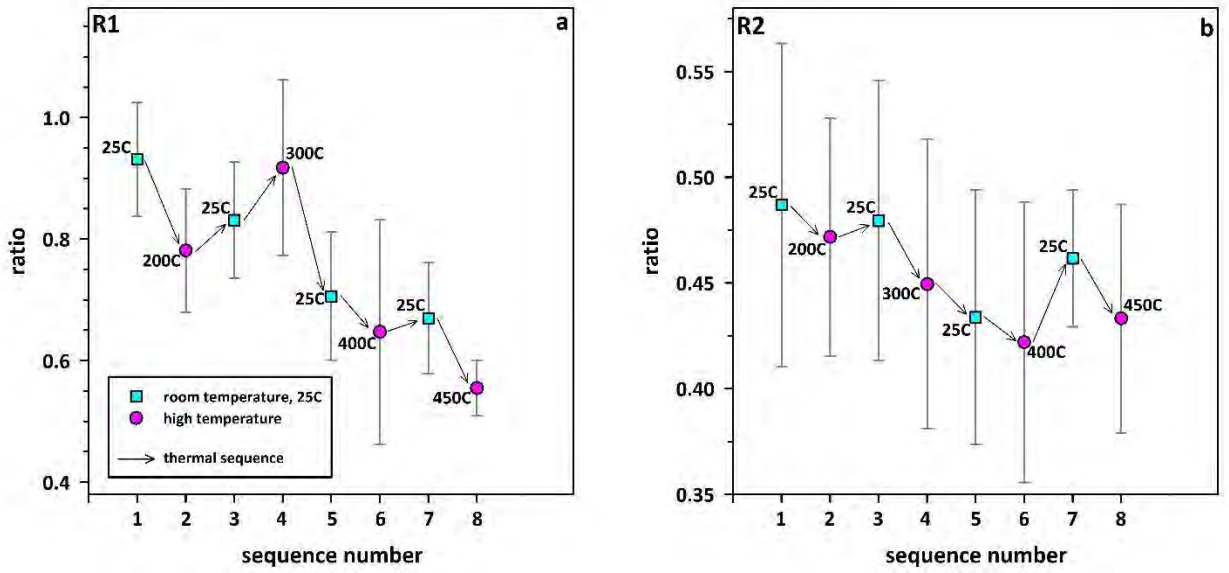

Figure 12. Temperature cycling experiments at room pressure show irreversible effects of heating on the R1 and R2 ratios at room temperature (blue shaded squares) prior to and following heating (pink shaded circles) to the temperatures indicated along a heating-cooling thermal

Figure 13

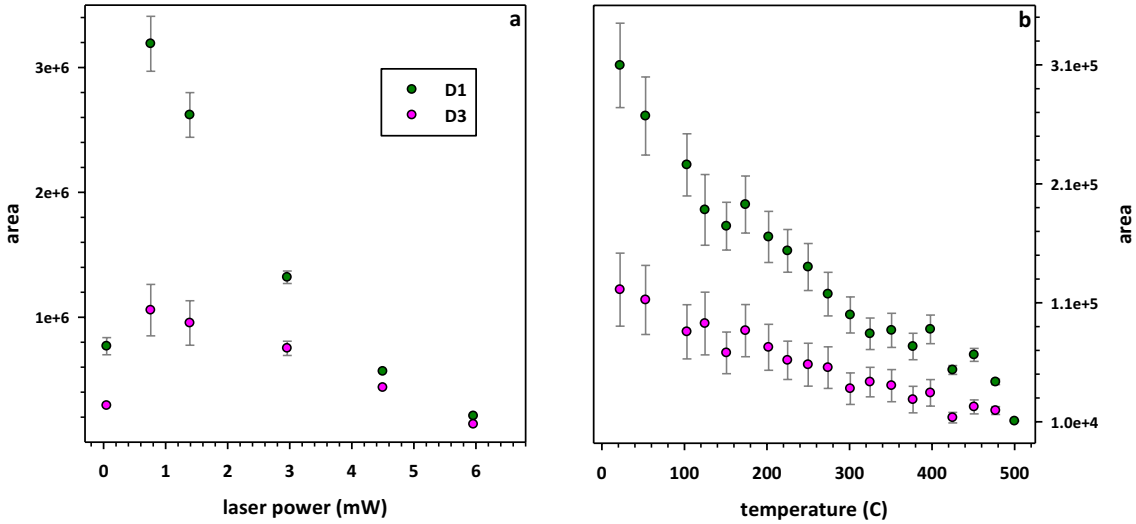

Figure 13. Area of disordered D1 and D3 bands as a function of laser power (a) and temperature (b), measured at 0.05 mW laser power at the sample.

877

878 **Figure 14**

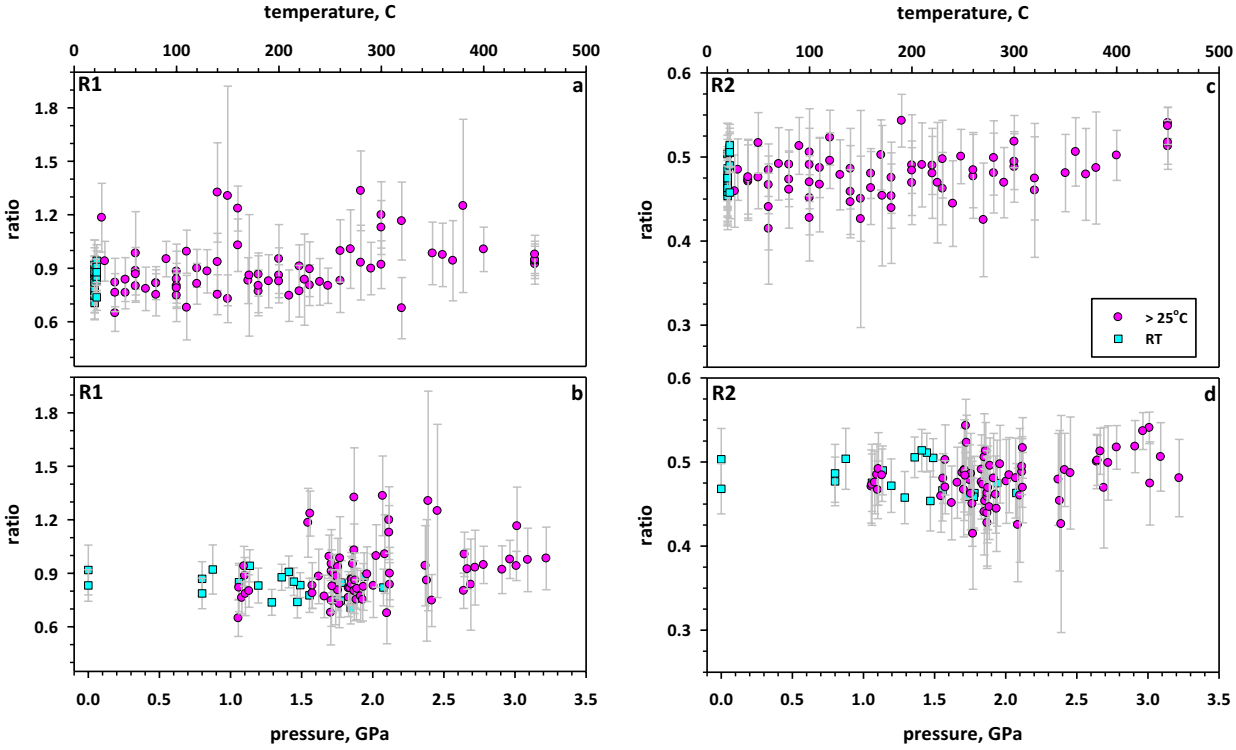

879

880 Figure 14. R1 (a,b) and R2 (c,d) ratios of kerogen spectra at high pressure and high temperatures.
881 Data measured at high temperature are shown by pink shaded circles, and data measured at room
882 temperature are shown blue shaded squares. In contrast to heating at room pressure, where the
883 R1 and R2 ratios decrease with increasing temperature (see Figure 9), at high pressures (>1 GPa)
884 there is no discernable variation in R1 and R2 as a function of temperature up to 450 °C.

885

886

887

888

889

890

891

892 **Figure 15**

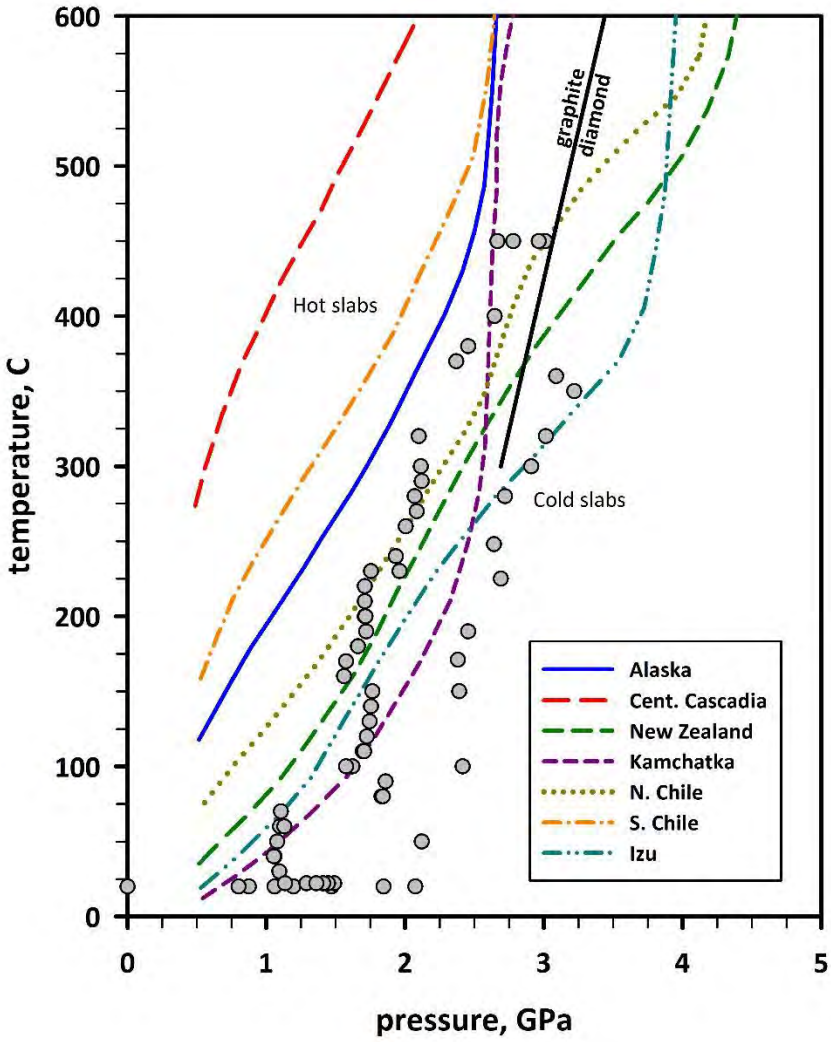

893

894 Figure 15. Pressure-temperature points visited in the current experiments in comparison to
895 several calculated geotherms in subducted slabs (Syracuse et al. 2010) along oceanic-continental
896 crust. The graphite-diamond phase boundary is shown by the solid black line (Kennedy and
897 Kennedy 1976). The structural integrity of kerogen to the highest P-T condition indicates that
898 instantaneous breakdown of kerogen will not occur in the upper part of slabs, potentially leading
899 to deeper subduction of carbon back into the mantle.